# Effect of Pressure-Assisted Heat Treatment on Photoluminescence Emission of α-Bi$_2$O$_3$ Needles

Samara Schmidt,[†] Evaldo T. Kubaski,[‡] Diogo P. Volanti,[§] Thiago Sequinel,[‖] Vinicius Danilo N. Bezzon,[†] Armando Beltrán,[∇] Sergio M. Tebcherani,[⊥] and José A. Varela[*,†]

[†]Department of Physical Chemistry, UNESP−Institute of Chemistry, 14800-060 Araraquara, SP Brazil

[‡]Department of Materials Engineering, State University of Ponta Grossa, 84030-900 Ponta Grossa, PR Brazil

[§]Department of Chemistry and Environmental Sciences, UNESP−IBILCE, 15054-000 São José do Rio Preto, SP Brazil

[‖]Department of Production Engineering, Federal University of Technology−Paraná, 84016-210 Ponta Grossa, PR Brazil

[⊥]Department of Chemistry, State University of Ponta Grossa, 84030-900 Ponta Grossa, PR Brazil

[∇]Departament de Química Física i Analítica, Universitat Jaume I, Campus del Riu Sec, E-12071 Castelló de la Plana, Spain

ⓢ *Supporting Information*

ABSTRACT: Materials with high photoluminescence (PL) intensity can potentially be used in optical and electronic devices. Although the PL properties of bismuth(III) oxide with a monoclinic crystal structure (α-Bi$_2$O$_3$) have been explored in the past few years, methods of increasing PL emission intensity and information relating PL emission to structural defects are scarce. This research evaluated the effect of a pressure-assisted heat treatment (PAHT) on the PL properties of α-Bi$_2$O$_3$ with a needlelike morphology, which was synthesized via a microwave-assisted hydrothermal (MAH) method. PAHT caused an angular increase between the [BiO$_6$]−[BiO$_6$] clusters of α-Bi$_2$O$_3$, resulting in a significant increase in the PL emission intensity. The Raman and XPS spectra also showed that the α-Bi$_2$O$_3$ PL emissions in the low-energy region (below ∼2.1 eV) are attributed to oxygen vacancies that form defect donor states. The experimental results are in good agreement with first-principles total-energy calculations that were carried out within periodic density functional theory (DFT).
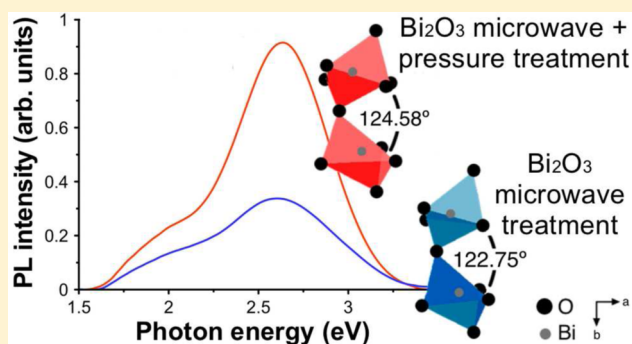
INTRODUCTION

Recently, bismuth(III) oxide (Bi$_2$O$_3$) has become a promising candidate for a variety of applications, because of its properties, such as a variable band gap (from 2.0 eV to 3.96 eV), photoconductivity, photoluminescence (PL), high refractive index, dielectric permittivity, and oxygen conductivity.[1,2] Despite the great technological interest in Bi$_2$O$_3$, some of its optical and electronic properties are not well-known. One of the problems associated with Bi$_2$O$_3$ studies is the existence of four main polymorphic phases that exhibit distinct properties: α (monoclinic), β (tetragonal), γ (body-centered cubic), and δ (face-centered cubic). The stable phase at room temperature is α-Bi$_2$O$_3$, while the high-temperature phase is δ-Bi$_2$O$_3$ that stabilizes at ∼730 °C and melts at 824 °C. The γ-Bi$_2$O$_3$ and β-Bi$_2$O$_3$ phases form at temperatures below 639 and 650 °C, respectively. The formation of β-Bi$_2$O$_3$ depends on impurities and oxide reaction conditions. Both the γ- and β-phases are metastable and can be obtained by controlled cooling during the process of crystal growth.[2,3] For example, Harwig and Gerards[4] showed the formation γ- and β-phases using cooling rates of 0.1 and 33 °C min^{-1}. They also provided a detailed

study on the formation of metastable phases of Bi$_2$O$_3$ at different cooling rates.

Depending on the method of preparation, α-Bi$_2$O$_3$ can contain traces of a secondary phase, which can contribute to the bulk properties of the oxide, because its polymorphs have a distinct nature. In some cases, the presence of a secondary phase impedes adequate control of the properties of Bi$_2$O$_3$ and makes the technological application of this oxide difficult.[5] Therefore, the evaluation of the phases that are present and their possible transitions are important topics related to the potential uses of this material.[6] Furthermore, the combination of powder X-ray diffraction (XRD) and the Rietveld Method (RM)[7] allows for evaluation of the possible structural variations in α-Bi$_2$O$_3$.

The PL behavior of Bi$_2$O$_3$ has been investigated over the past few years, because of the different optical applications of this oxide.[6,8,9] Most results are explained by the fact that the band-gap values are dependent on different phases or on the particle size of nanostructures.[10,11] The PL spectra of α-Bi$_2$O$_3$

microcrystals generally show a band at 2.8 eV attributed to a recombination between valence and conduction bands, and a band at 2.98 eV, which corresponds to surface state interactions. α-Bi_2O_3 nanoparticles show a band of PL emission at 3.12 eV.[6,9] For α-Bi_2O_3 ceramics, the PL emission consisted of three bands with maxima at 2.70, 2.40, and 1.97 eV; these bands were associated with complexes containing closely packed bismuth and oxygen in the crystal structure.[11,12] Unlike for other oxides of technological interest, information regarding PL emission in α-Bi_2O_3 related to native defects or other types of defects is still scarce.[13] Furthermore, low-energy PL emissions (below ~2.1 eV) are explained in terms of oxygen defects and bismuth oxidation states.[6,11,14] Materials with increased PL properties are of interest, and obtaining a higher PL emission at a low synthesis temperature is important to decrease costs in several electronic and optical devices.

Pressure-assisted heat treatment (PAHT) was successfully used to prepare calcium copper titanate ($CaCu_3Ti_4O_{12}$, CCTO)[15] and zinc oxide (ZnO) thin films.[16] In CCTO films, PAHT caused a decrease in the band gap, moving the PL emission to a lower energy region.[15] Similarly, in ZnO films, PAHT promoted a significant change in the level of defects, shifting the PL emission from green to orange-yellow.[16]

PAHT caused significant changes in the PL properties of CCTO[15] and ZnO[16] thin films, and it is hypothesized that a similar influence could be found in bulk α-Bi_2O_3. Based on these facts, the intent of this study is to investigate the effect of PAHT on the PL properties of α-Bi_2O_3 needles synthesized by the microwave-assisted hydrothermal (MAH) method.

■ MATERIALS AND METHODS

Reactants. The reactants used in the experiments were bismuth-(III) nitrate pentahydrate ($Bi(NO_3)_3 \cdot 5H_2O$, Sigma−Aldrich, 99.99%), potassium hydroxide (KOH, J.T. Baker, 87.0%), nitric acid (HNO_3, Sigma−Aldrich, 65%), and polyethylene glycol (PEG-300, Sigma−Aldrich).

Microwave-Assisted Hydrothermal (MAH) Synthesis of α-Bi_2O_3. The bismuth solution was prepared by dissolving 2.19 g of $Bi(NO_3)_3 \cdot 5H_2O$ in 40 mL HNO_3 with continuous stirring. After complete dissolution, 2 mL of PEG-300 were added and the solution was stirred for 10 min. Then, a KOH solution (6 mol L^{-1}) was added dropwise with stirring until pH 14. The solution was stirred for 5 min, and the formation of a gelatinous white precipitate was observed. The solution and the precipitate were transferred to a polytetrafluoro-ethylene (PTFE) reactor and were placed in the MAH system for 30 min at 80 °C with a heating rate of 10 °C min^{-1}. After cooling the reactor to room temperature, the formation of a yellow precipitate was observed. The resulting material was washed six times with distilled water until pH ~7. After centrifugation, the powder was dried in Petri dishes at 70 °C for 24 h. Finally, the powder was calcined at 400 °C for 1 h at a heating rate of 10 °C min^{-1} to eliminate any trace of PEG-300, which could be adsorbed on the samples. Samples obtained by this route were labeled α-Bi_2O_3-MAH.

Pressure-Assisted Heat Treatment (PAHT). Samples of α-Bi_2O_3-MAH were heat-treated under an air pressure of 2 MPa at 120 °C for 48 h to evaluate the effect of PAHT on the PL properties of α-Bi_2O_3. Samples that underwent the pressure-assisted heat treatment were labeled α-Bi_2O_3-PAHT.

Sample Characterization. Powder samples of α-Bi_2O_3-MAH and α-Bi_2O_3-PAHT were characterized by X-ray diffraction (XRD) at room temperature, using a Rigaku Ultima IV diffractometer with Cu Kα radiation, a goniometer radius of 185 mm, a curved graphite monochromator, and a scintillation counter operating in the reflection mode with the Bragg−Brentano geometry. The divergence, scattering, and receiving slits were 0.5°, 0.5°, and 0.3 mm, respectively. Data were

collected over the 2θ measuring range of 15°−90° in the continuous scan mode (1°/min).

Refinements were carried out by the Rietveld method using fundamental parameters (FPs) implemented in the Topas Academic V.5 software.[17] FPs were used to describe the peak profile by executing the convolutions of functions in reference to the contribution of wavelength distribution, instrumental parameters of the geometry used, and sample physical properties. A silicon standard sample was used to obtain the instrumental broadening, which was corrected using FPs.[18] The background was adjusted using a Chebyshev polynomial function implemented in the software with four terms for correction. Lattice parameters and crystallite size were refined, and a spherical harmonics preferred orientation correction with eight terms was applied. Malmros[19] reported the crystalline structure used in these refinements. The values of the crystallite size were calculated using a macro implemented in the Topas Academic V.5 software;[17] the macro considers the integrated peak intensity to estimate the mean value of the crystallite size. After the refinements, CIF files were created for each sample to simulate material structures in the Diamond V.3.2e software.[20] In addition, interatomic distances with uncertainties were calculated using the Bond_Str program.[21]

Morphological features of the samples were analyzed by field-emission scanning electron microscopy (FESEM), using a JEOL Model 7500F instrument. Samples were dispersed in isopropyl alcohol with the assistance of an ultrasound bath. A drop of this suspension was deposited on a conductive silicon substrate, and the sample was dried at room temperature before FESEM analysis.

PL measurements of α-Bi_2O_3-MAH and α-Bi_2O_3-PAHT were performed with a Thermo Jarrel Ash Monospec (27 cm) monochromator coupled to an R955 Hamamatsu photomultiplier, using a krypton ion laser (Coherent Innova 200) operating at a wavelength of 350 nm and 60 mW output power. The PL spectra were obtained as a function of wavelength and were converted to photon energy (eV), and each PL intensity was multiplied by λ^2 to obtain the corrected intensity.[22,23] Deconvolution analyses of PL spectra were performed using the Peakfit Program (version 4.05);[24] a Gaussian function was used to adjust the PL bands to determine peak positions and their corresponding areas. The least number of Gaussian emissions necessary to obtain the best fit in plots was used, and each parameter was fitted for each spectrum independently. The contribution of each PL band was estimated in terms of its area, which was expressed as a percentage. Ultraviolet−visible (UV-vis) absorption spectra were obtained using a Varian Cary 50 spectrophotometer to determine the band gap of α-Bi_2O_3-MAH and α-Bi_2O_3-PAHT; the band gap was estimated using the Kubelka−Munk method.[25] All these characterizations were performed at room temperature.

Raman spectroscopy was used to estimate short- and medium-range order, crystal potential fluctuations, and local atomic arrangement of samples, and as an auxiliary technique to investigate changes in crystal symmetry that can be caused by PAHT. Raman spectra were obtained by a spectrometer equipped with a Kimmon set of mirrors. Measurements were obtained for solid samples at room temperature using a He-Cd laser with a wavelength of 514 nm. Scans were obtained over the range of 100−600 cm^{-1}.

The chemical states of the elements in α-Bi_2O_3-MAH and α-Bi_2O_3-PAHT were characterized by X-ray photoelectron spectroscopy (XPS), using a UNI-SPECS UHV System commercial spectrometer at a pressure below 5 × 10^{-7} Pa. The Mg Kα line (energy of 1253.6 eV) was used as the ionization source and the pass energy of the analyzer was set to 10 eV. The inelastic background of the high-resolution spectra Bi 4f, C 1s, and O 1s orbitals was subtracted using the Shirley method.[26] The spectral binding-energy scale was corrected using the hydrocarbon component fixed at 285.0 eV. The width at half height varied between 1.2 and 2.1 eV, and the peak position were determined with a precision of ±0.1 eV.

Theoretical Calculation. First-principles total-energy calculations were carried out within periodic density functional theory (DFT), using CRYSTAL14 program package.[27] The Kohn−Sham equations have been solved by means of exchange−correlation functionals in the generalized gradient approximation (GGA) developed for solids by

Perdew, Burke, and Ernzerhof (PBESol).[28] The Bi and O centers have been described in the scheme [PS]-41G* and 6-31G*, respectively, where [PS] stands for the nonrelativistic effective core pseudo-potential. Both the [PS]-41G* and 6-31G* basis sets can be found at http://www.crystal.unito.it/basis-sets.php. Geometrical parameters and internal positions were optimized at both ambient pressure and 2 MPa (EXTPRESS option).

■ RESULTS AND DISCUSSION

Both α-Bi_2O_3-MAH and α-Bi_2O_3-PAHT samples showed a pure α-Bi_2O_3 phase, as determined from the XRD data and Rietveld plots that are depicted in Figure 1. Table 1 shows the
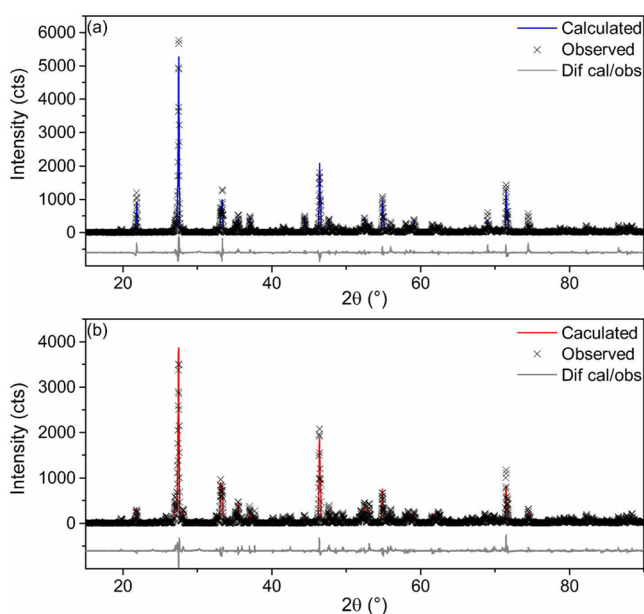
Figure 1. Rietveld plots of the samples: (a) α-Bi_2O_3-MAH and (b) α-Bi_2O_3-PAHT.

values of the lattice parameters and atomic positions obtained after the refinements. This table also presents the agreement factors of the refinements. Although these numeric criteria are slightly high, Young[29] reported that it is also necessary to consider graphical criteria. Consequently, a careful evaluation of Figures 1a and 1b indicate an adequate adjustment between the observed and calculated profiles.

The comparison between the results of the two samples shows a slight variation in atomic position, especially for the oxygen sites. This variation is probably due to the synthesis method used for sample α-Bi_2O_3-MAH. PAHT virtually caused no alteration in the lattice parameters of the samples; the cell volume was the same for both samples. In addition, the crystallite size was another parameter that showed no variation, because both samples showed the same order of magnitude.

The Diamond software[20] allowed simulation of the material structure, the coordination of the Bi and O atoms, and measurement of the angle between the coordination polyhedra. The simulations showed changes in the relative distance of separation between atoms when both α-Bi_2O_3-MAH and α-Bi_2O_3-PAHT are compared (see Table 2), although the coordination of the polyhedra had been preserved. α-Bi_2O_3-PAHT shows that the relative angles between clusters [BiO_6]-[BiO_6] were greater than in α-Bi_2O_3-MAH (Figure 2).

Figure 3 depicts the needlelike morphological features of α-Bi_2O_3-MAH and α-Bi_2O_3-PAHT analyzed by FESEM. It was

Table 1. Refined Structural Parameters and the Respective Agreement Factors of the Refinement

Space Group $P2_1/c$	
α-Bi_2O_3-MAH	**α-Bi_2O_3-PAHT**

Lattice Parameters	**Lattice Parameters**
a = 5.8480(6) Å	a = 5.8484(3) Å
b = 8.1690(10) Å	b = 8.1687(5) Å
c = 7.5131(8) Å	c = 7.5133(4) Å
α = 90°	α = 90°
β = 112.970(7)°	β = 112.992(4)°
volume = 330.46 Å³	volume = 330.42 Å³

Atomic Positions			
Bi1 site	*Bi2 site*	*Bi1 site*	*Bi2 site*
x = 0.5244(8)	x = 0.0410(7)	x = 0.5246(7)	x = 0.0410(6)
y = 0.18332(17)	y = 0.04082(18)	y = 0.1819(2)	y = 0.0423(2)
z = 0.3573(6)	z = 0.7799(8)	z = 0.3584(5)	z = 0.7781(6)
Beq^a = 0.40(4) Å²	Beq^a = 0.92(4) Å²	Beq^a = 0.70(6) Å²	Beq^a = 0.83(7) Å²
O1 site	*O2 site*	*O1 site*	*O2 site*
x = 0.818(9)	x = 0.260(3)	x = 0.815(8)	x = 0.261(9)
y = 0.303(2)	y = 0.044(3)	y = 0.297(2)	y = 0.048(2)
z = 0.768(10)	z = 0.133(10)	z = 0.751(8)	z = 0.174(7)
O3 site		*O3 site*	
x = 0.294(9)		x = 0.329(9)	
y = 0.033(3)		y = 0.015(3)	
z = 0.448(9)		z = 0.513(7)	

Agreement Factors	**Agreement Factors**
R_{Bragg} = 7.35%	R_{Bragg} = 8.00%
R_{wp} = 22.60%	R_{wp} = 22.52%
R_{exp} = 11.99%	R_{exp} = 12.25%
S = 1.88	S = 1.84

| **Crystallite Size**	**Crystallite Size**
137(5) nm	117(4) nm

^{a}Beq = temperature factor. The temperature factors for oxygen atoms were constrained during the refinement following the values presented by Malmros.[19]

Table 2. Interatomic Distances with Uncertainties between Bi and O atoms in the α-Bi_2O_3 Simulated Structures

Interatomic Distances (Å)			
α-Bi_2O_3-MAH		**α-Bi_2O_3-PAHT**	
B1		**B1**	
O1	3.05(6)	O1	2.93(5)
O1	2.08(7)	O1	2.15(6)
O2	2.12(4)	O2	1.96(4)
O2	3.19(3)	O2	3.29(3)
O3	2.12(6)	O3	2.36(5)
O3	2.28(4)	O3	1.90(3)
B2		**B2**	
O1	2.49(3)	O1	2.43(3)
O1	2.19(4)	O1	2.22(3)
O2	2.45(7)	O2	2.74(5)
O2	2.21(5)	O2	2.07(6)
O3	3.36(7)	O3	3.08(6)
O3	2.12(4)	O3	2.45(4)

found that pure α-Bi_2O_3 needles could be obtained for MAH, using an alkaline KOH solution (6 mol L⁻¹). The as-prepared α-Bi_2O_3 needles are nonagglomerated particles; the length of the needles range from 13 to 41 μm, and the aspect ratio of the needles range from 9 to 14 (Figure 3a). Furthermore, a
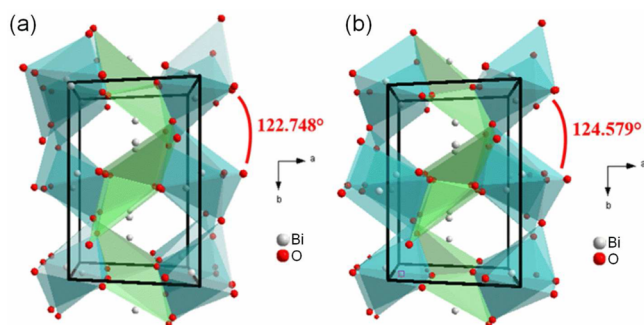
Figure 2. Coordination polyhedra for α-Bi_2O_3 in the simulated structures: (a) α-Bi_2O_3-MAH and (b) α-Bi_2O_3-PAHT.
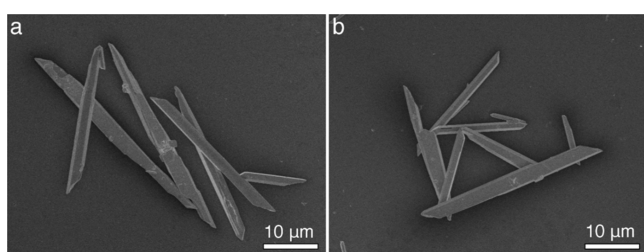
Figure 3. FESEM images using secondary electrons: (a) α-Bi_2O_3-MAH and (b) α-Bi_2O_3-PAHT.

morphological analysis of the particle surfaces shows that PAHT caused no significant alteration (Figure 3b).

Figure 4 shows a comparison of the PL emission between α-Bi_2O_3-MAH and α-Bi_2O_3-PAHT. The maximum PL emission
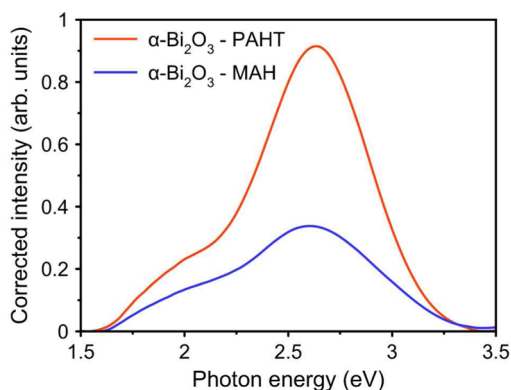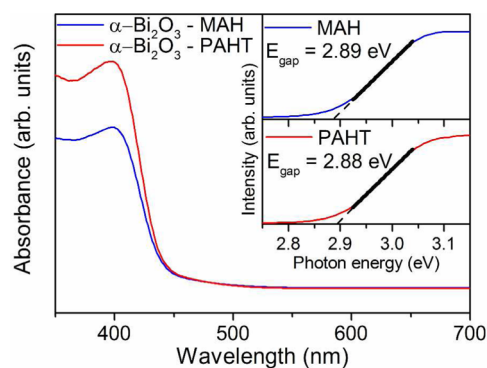

Figure 4. PL emission of α-Bi_2O_3-MAH and α-Bi_2O_3-PAHT.

occurred at ~2.7 eV (blue region) for both samples. After pressure treatment, a substantial increase in the PL intensity was observed. The PL bands were deconvoluted to evaluate which electronic transitions influence the PL response. The deconvolution of PL spectra is shown in Figure 5. The PL emission in both samples is composed of five components ranging between 1.77 eV (red) and 3.05 eV (violet), and the spectra were deconvoluted as 1.89, 2.15, 2.50, 2.77, and 3.05 eV, and 1.77, 1.96, 2.28, 2.60, and 2.85 eV for α-Bi_2O_3-MAH and α-Bi_2O_3-PAHT, respectively.

Figure 6 shows the UV-vis absorption spectra of α-Bi_2O_3-MAH and α-Bi_2O_3-PAHT, and an estimate of the band gap (E_{gap}) for direct transitions, which was calculated using the Kubelka–Munk[25] method. The deconvolution shown in Figure 5 reveals that the PL emissions with the highest energy levels
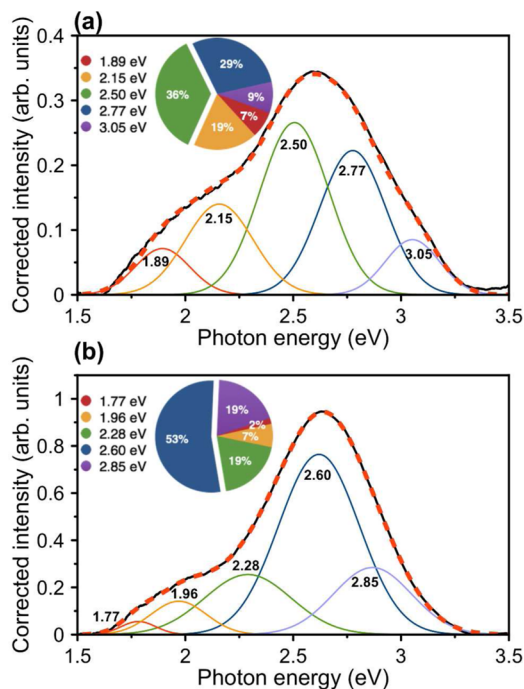
Figure 5. Deconvolution of PL spectra: (a) α-Bi_2O_3-MAH and (b) α-Bi_2O_3-PAHT. The dotted lines in panels (a) and (b) are the sum of the deconvolution peaks. The correlation coefficient for both calculated fits is $R^2 = 0.998$.

**Figure 6.** UV-vis absorption spectra and estimation of the band gap.

occurred at ~3.05 and ~2.85 eV (violet region) for α-Bi_2O_3-MAH and α-Bi_2O_3-PAHT, respectively. These emissions can be related to the direct transitions between the conduction and valence bands, since the band-gap energies for both samples were estimated as 2.89 and 2.88 eV. These band gap values are close to those found in most literature reports (2.85 eV) for α-Bi_2O_3 structures.[9−11] The band gap of α-Bi_2O_3-MAH estimated using the Kubelka–Munk method is slightly lower than the corresponding value for the direct transitions found in PL deconvolution; other works[6,11] reported a similar effect. Furthermore, PAHT promoted an increase in the contribution of the spectral range related to the direct transitions between the conduction and valence bands. Figure 5 shows that the contribution of this band changed from 9% (3.05 eV) in α-Bi_2O_3-MAH to 19% (2.85 eV) in α-Bi_2O_3-PAHT.

Trivalent Bi ions in inorganic compounds exhibit PL properties related to their $6s^2$ levels. The luminescence of Bi^{3+} ions appears in the blue-green region of the spectrum and is attributed to the $^3P_1-^1S_0$ transitions or charge transfer

between the bonding oxygen and Bi^{3+} ions.[10,11,13] In α-Bi_2O_3-MAH, the bands associated with the blue-green emission corresponded to 65% of the total emission (29% was attributed to the blue region (2.77 eV), while 36% was attributed to the green region (2.50 eV)). α-Bi_2O_3-PAHT showed an increase in PL in the blue-green spectral range to 72%, and an increase in the band relative to the blue component; in this case, 53% was related to the blue region (2.60 eV) and 19% to the green region (2.28 eV).

Figures 4 and 5 also show PL emission in the low-energy region, and, in this case, PAHT showed a significant decrease in the emission of this region related to the total PL emission. α-Bi_2O_3-MAH has 19% of its emission at 2.15 eV and 7% at 1.89 eV that correspond to 26% of the total emission, while α-Bi_2O_3-PAHT has 7% of its emission at 1.96 eV and 2% at 1.77 eV, which correspond to only 9% of the total PL emission of α-Bi_2O_3-PAHT. The luminescence in the low-energy spectral range is normally attributed to the $^2P_{3/2}$–$^2P_{1/2}$ transition of Bi^{2+} ions.[8,10] However, recent works[11,30] reported that the emission in the low-energy spectral range is attributed to the structural defects of oxygen (oxygen vacancies). Wu and Lu[30] also associated the PL emission at this spectral range to oxygen vacancies and stated that the higher the emission intensity at this spectral range, the greater the vacancy density. Therefore, in order to determine the cause for the PL emission at this spectral range, it is necessary to verify the existence of Bi^{2+} ions on the material surface. In the present work, the presence or absence of Bi^{2+} ions in samples was tested using Raman and XPS spectra.

Raman characteristics of α-Bi_2O_3 are well-known.[31] For the α-Bi_2O_3 monoclinic structure with space group $P21/c$ and 4 formula units or 20 atoms per unit cell, analyses predict 30 active Raman modes ($15Ag + 15Bg$), but only a fraction of these modes is generally observed.[11] The Raman spectra in Figure 7 show 10 prominent Raman bands for both samples at
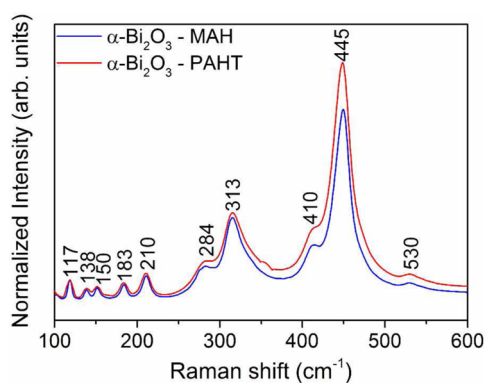

Figure 7. Raman spectra of α-Bi_2O_3-MAH and α-Bi_2O_3-PAHT samples.

117, 138, 150, 183, 210, 284, 313, 410, 445, and 530 cm^{-1}, which are in agreement with bands found in the literature for α-Bi_2O_3.[6,11,32] The band at 117 cm^{-1} is attributed to the vibration mode of bismuth while bands at 138 and 150 cm^{-1} refer to Bi–O scattering. Furthermore, all other bands were attributed to oxygen vibrations, which are broader than bands observed at 117, 138, and 150 cm^{-1}, and demonstrate a strong anharmonicity of oxygen vibration modes. Bands related to neither another Bi_2O_3 phase nor Bi^{2+} were detected for both α-Bi_2O_3-MAH and α-Bi_2O_3-PAHT.

A detailed comparison between the Raman spectra of α-Bi_2O_3-MAH and α-Bi_2O_3-PAHT in the low-frequency range shows no relevant spectral changes. On the other hand, for frequencies higher than 284 cm^{-1}, α-Bi_2O_3-PAHT showed an increase in the spectrum intensity compared to α-Bi_2O_3-MAH. These different intensities can be associated with changes in the electronic density of the crystal, which also modifies the PL properties. The effect of intensity change in the Raman spectra has already been observed in other materials. For example, a change in the intensity of the Raman spectra was observed for $CaTiO_3$ perovskite-based materials obtained by MAH,[33] and for irregular cube-like $(Ca_{1-x}Cu_x)TiO_3$ microcrystals also synthesized by MAH.[34] In both studies, the authors showed that a change in the cluster angles promoted variations in intensities of the Raman spectra, which were attributed to changes in the average electronic density of the crystal, and could modify the PL properties. In addition, these authors used XRD and Rietveld refinements to measure the cluster angles in their samples.[33,34] In the present work, the increase in Raman spectra intensity was caused by an increase in the average electronic density, which was promoted by the change in the angles between clusters $[BiO_6]$–$[BiO_6]$. Consequently, the intensity increase in the Raman spectra observed in α-Bi_2O_3–PAHT is explained by a structural disorder caused by the increase in the relative angles between clusters $[BiO_6]$–$[BiO_6]$. Results of three experimental and theoretical studies[35−37] on the structural properties of α-Bi_2O_3 under high pressures, which also demonstrated that pressure promotes a distortion in clusters $[BiO_6]$–$[BiO_6]$, supports the results presented in this work.

The chemical states of the elements in the α-Bi_2O_3-MAH and α-Bi_2O_3-PAHT samples were also characterized by XPS, and Figure 8 depicts these results. Figures 8a and 8b show the XPS spectra obtained for α-Bi_2O_3-MAH and α-Bi_2O_3-PAHT, respectively. Figures 8c and 8d show the Bi 4f levels, while Figures 8e and 8f show the O 1s levels for both samples.

XPS results indicated that the surfaces of both samples are composed of Bi_2O_3. Carbon peaks found in the XPS spectra (Figures 8a and 8b) can be attributed to contamination due to
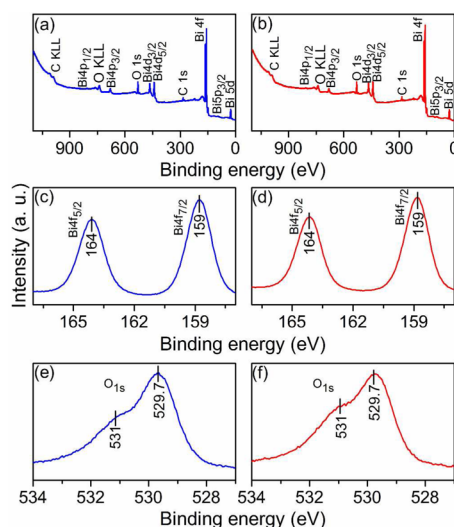
Figure 8. XPS spectra of samples (a) α-Bi_2O_3-MAH and (b) α-Bi_2O_3-PAHT. XPS spectra of Bi $4f_{7/2}$ and Bi $4f_{5/2}$ levels for (c) α-Bi_2O_3-MAH and (d) α-Bi_2O_3-PAHT. XPS spectra of O 1s levels for (e) α-Bi_2O_3-MAH and (f) α-Bi_2O_3-PAHT.
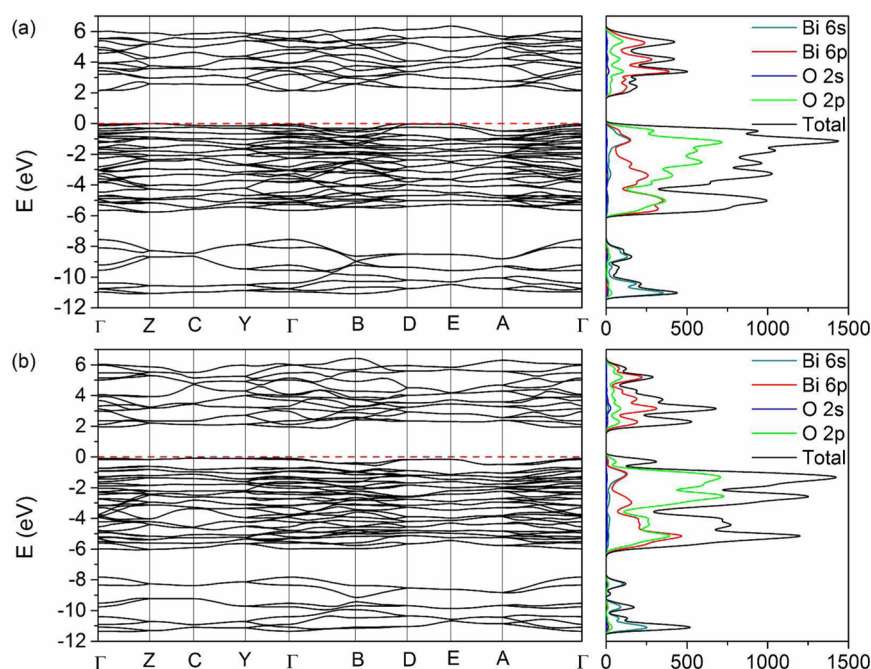
Figure 9. Electronic band structures and partial electron density of states for (a) α-Bi$_2$O$_3$-MAH (ambient pressure) and (b) α-Bi$_2$O$_3$-PAHT (pressure of 2 MPa). The top of the valence band is set to 0 on the vertical axis.

exposure to the atmosphere.[38] Figures 8c and 8d present the spin orbit splitting for pure Bi 4f$_{7/2}$ and Bi 4f$_{5/2}$ with binding energies of 159 and 164 eV, respectively. In addition, the spin orbit splitting with these binding energies values is a characteristic of Bi^{3+} ions in α-Bi$_2$O$_3$.[39]

The XPS profiles of O 1s levels (Figures 8e and 8f) show a dominant peak at 529.7 eV, whose binding energy is a characteristic of oxygen in Bi$_2$O$_3$ (structural oxygen). The binding energy at 531 eV could be attributed to the surface oxygen present as hydroxyl groups (OH$^-$).[39,40] The hydroxyl groups could originate when the samples are exposed to air or could be adsorbed during the MAH synthesis in an alkaline medium.

Raman spectroscopy and XPS did not detect any signal indicating the presence of Bi^{2+} ions in α-Bi$_2$O$_3$-MAH and α-Bi$_2$O$_3$-PAHT. These results suggest that the PL emission in the low-energy region (below ~2.1 eV) is due to oxygen vacancies that form defect donor states, and this PL is composed of many defect donor states to valence band emissions.[3] The oxygen vacancy states may contain Bi centers in other oxidation states, including Bi^{2+}, which can emit PL from red to blue emission.[41] The present work shows that emission in the low-energy region (below ~2.1 eV) can be attributed to oxygen vacancies that were coherently reduced after PAHT. These results are in good agreement with reports from the literature stating that the PL emission at this region is explained in terms of oxygen defects and bismuth oxidation states.[6,11,14] However, XPS results presented in the work of Vila et al.[6] showed the presence Bi^{2+} on sample surface while in the present work Raman and XPS results showed no signal of Bi^{2+}.

The calculated bulk Bi$_2$O$_3$ band structures along the adequate symmetry lines of the monoclinic $C2/m$ Bravais lattice and the density of states (DOS) total and projected on most relevant atomic orbitals for the two Bi$_2$O$_3$ samples are shown in Figure 9. The theoretical calculations render for the α-Bi$_2$O$_3$-MAH structure that the valence band (VB) maximum and conduction band (CB) minimum are located at Z and near

Γ (actually in the line between Γ and Y but close to Γ) k-points. The calculated band gap is 2.149 eV close to the direct band gap at Γ of 2.194 eV. The α-Bi$_2$O$_3$-PAHT band structure presents also an indirect gap of 1.919 eV from the vicinity of Γ to a point between Γ and B k-points also close to the direct gap at Γ of 2.059 eV.

It is well-known that Local Density (LDA) and Generalized Gradient Approximation (GGA) density functionals generally underestimate band gaps for semiconductors. Taking this fact into account, our results compare well with the calculated indirect band gap of 2.45 eV at ambient pressure, using the GGA-PBE[42] method and with and the experimental value of 2.5 eV[43] and with our experimental value of 2.88–2.89 eV. Our calculations predict for both α-Bi$_2$O$_3$-MAH and α-Bi$_2$O$_3$-PAHT structures that the top of the VB is derived mostly from the O 2p state and, in less measure, the Bi 6p and 6s states, suggesting a slight hybridization of the Bi 6s and Bi 6p orbitals, while in the bottom of CB, the Bi 6p state dominates over the O 2p contribution state. Therefore, the photoelectron mainly transfers from O 2p and Bi 6s–6p in the top of the VB to Bi 6p in the bottom of CB. The decrease in the α-Bi$_2$O$_3$-PAHT band gap energy is due to an increase of the Fermi energy and a slight decrease of its CB minimum.

Upon comparing the PL emission of α-Bi$_2$O$_3$-MAH and α-Bi$_2$O$_3$-PAHT (Figure 4), the latter showed an increase in the PL intensity. The pressure-assisted heat treatment of α-Bi$_2$O$_3$-MAH needles caused an increase in the angle between [BiO$_6$]–[BiO$_6$] clusters, which promoted an increase in the electronic density of the material, which was considered as the cause for the increase in PL emission intensity. On the other hand, the contribution of PL emission in the low-energy range to the total PL emission is considerably greater in α-Bi$_2$O$_3$-MAH than in α-Bi$_2$O$_3$-PAHT. This is mainly because α-Bi$_2$O$_3$-PAHT suffered the pressure-assisted heat treatment under air atmosphere (rich in oxygen). Consequently, under higher oxygen pressure, the formation of oxygen vacancies that form the defect donor states was disadvantageous.

Article

Theoretical results showed that O 2p states have an important role in photoelectron transfers in both samples. For both α-Bi_2O_3-MAH and α-Bi_2O_3-PAHT, the top of VB is mainly composed of O 2p states, which are predominantly influenced by changes on axial oxygen atoms of $[BiO_6]$ octahedra. The axial oxygen atoms are directly involved in the angles between $[BiO_6]$–$[BiO_6]$ clusters that were greater in α-Bi_2O_3-PAHT than in α-Bi_2O_3-MAH. Rietveld refinements already showed the difference in cluster angles of samples (Figure 2). In addition, the change in cluster angle can directly change the polarization of O 2p states, and, consequently, their interaction with Bi 6p states. As a result, the change in the angles between $[BiO_6]$–$[BiO_6]$ clusters promote an increase in the electronic density of crystal and the increase in the PL intensity. These findings are in good agreement with the discussion on Raman spectra (Figure 7), which shows an increase in the electronic density of α-Bi_2O_3-PAHT.

CONCLUSIONS

The pressure-assisted heat treatment of α-Bi_2O_3-MAH needles caused an intrinsic disorder characterized by an increase in the angle between the $[BiO_6]$–$[BiO_6]$ clusters. This angular increase promoted a significant rise in the electronic density of the material, which was considered as the cause for the increase in PL emission intensity in the blue region. Consequently, the origin of the structure with higher electronic density and the increase in PL emission intensity are due to the structural distortion related to the $[BiO_6]$–$[BiO_6]$ clusters. In addition, the PL emissions of α-Bi_2O_3 in the low-energy region (below ~2.1 eV) can be attributed to oxygen defects (oxygen vacancies) that form defect donor states; this PL comprises defect states to valence band emissions. Theoretical calculation is in good agreement with the experimental findings. Theoretical results showed that O 2p states have an important role in photoelectron transfers in both samples. The change in the angle between the $[BiO_6]$–$[BiO_6]$ clusters can change the polarization of O 2p states and, consequently, change the electronic density of crystals.

ASSOCIATED CONTENT

ⓈSupporting Information

The Supporting Information is available free of charge on the ACS Publications website at DOI: 10.1021/acs.inorg-chem.5b01237.

> Deconvolution of XPS spectra (PDF)
> CIF data for α-Bi_2O_3 produced via microwave-assisted hydrothermal (MAH) treatment (CIF)
> CIF data for α-Bi_2O_3 produced via pressure-assisted heat treatment (PAHT) (CIF)

AUTHOR INFORMATION

Corresponding Author
*Tel.: +55 16 3301-9892. E-mail: varela@iq.unesp.br.
Notes
The authors declare no competing financial interest.

ACKNOWLEDGMENTS

REFERENCES

(1) Ismail, R. A.; Fadhil, F. A. J. Mater. Sci.: Mater. Electron. **2014**, 25, 1435−1440.
(2) Yang, G. B.; Li, Y. X.; Yin, Q. R.; Wang, P. L.; Cheng, Y. B. Mater. Lett. **2002**, 55, 46−49.
(3) Ho, C. H.; Chan, C. H.; Huang, Y. S.; Tien, L. C.; Chao, L. C. Opt. Express **2013**, 21, 11965−11972.
(4) Harwig, H. A.; Gerards, A. G. Thermochim. Acta **1979**, 28, 121−131.
(5) Huang, L.; Li, G.; Yan, T.; Zheng, J.; Li, L. New J. Chem. **2011**, 35, 197−203.
(6) Vila, M.; Diaz-Guerra, C.; Piqueras, J. J. Alloys Compd. **2013**, 548, 188−193.
(7) Rietveld, H. J. Appl. Crystallogr. **1969**, 2, 65−71.
(8) Tien, L.-C.; Lai, Y.-C. Appl. Surf. Sci. **2014**, 290, 131−136.
(9) Xiong, Y.; Wu, M.; Ye, J.; Chen, Q. Mater. Lett. **2008**, 62, 1165−1168.
(10) Wang, Y.; Zhao, J.; Zhou, B.; Zhao, X.; Wang, Z.; Zhu, Y. J. Alloys Compd. **2014**, 592, 296−300.
(11) Vila, M.; Diaz-Guerra, C.; Piqueras, J. Mater. Chem. Phys. **2012**, 133, 559−564.
(12) Bordun, O. M.; Kukharskii, I. I.; Dmitruk, V. V.; Antonyuk, V. G.; Savchin, V. P. J. Appl. Spectrosc. **2008**, 75, 681−684.
(13) Boutinaud, P. Inorg. Chem. **2013**, 52, 6028−6038.
(14) Vila, M.; Diaz-Guerra, C.; Piqueras, J.; Lopez-Conesa, L.; Estrade, S.; Peiro, F. CrystEngComm **2015**, 17, 132−139.
(15) Sequinel, T.; Garcia, I. G.; Tebcherani, S. M.; Kubaski, E. T.; Oliveira, L. H.; Li, M. S.; Longo, E.; Varela, J. A. J. Alloys Compd. **2014**, 583, 488−491.
(16) Berger, D.; Kubaski, E. T.; Sequinel, T.; da Silva, R. M.; Tebcherani, S. M.; Varela, J. A. Luminescence **2013**, 28, 942−947.
(17) Coelho, A. Topas Academic, version 5; Coelho Software: Brisbane, Australia, 2012.
(18) Cheary, R.; Coelho, A.; Cline, J. P. J. Res. Natl. Inst. Stand. Technol. **2004**, 109, 1−25.
(19) Malmros, G.; Fernholt, L.; Ballhausen, C. J.; Ragnarsson, U.; Rasmussen, S. E.; Sunde, E.; Sørensen, N. A. Acta Chem. Scand. **1970**, 24, 384−396.
(20) Putz, H.; Brandenburg, K. Diamond—Crystal and Molecular Structure Visualization, version 3.2; Crystal Impact: Bonn, Germany, 2010.
(21) Rodríguez-Carvajal, J. Phys. B (Amsterdam, Neth.) **1993**, 192, 55−69.
(22) Hamilton, T. D. S.; Munro, I. H.; Walker, G. Luminescence Instrumentation. In Luminescence Spectroscopy, Lumb, M. D., Ed.; Academic Press: London, 1978; pp 149−238.
(23) Kalceff, M. A. S.; Phillips, M. R. Phys. Rev. B: Condens. Matter Mater. Phys. **1995**, 52, 3122−3134.
(24) PeakFit, version 4.12; Systat Software, Inc.: San Jose, CA, .
(25) Kubelka, P.; Munk-Aussig, F. Z. Tech. Phys. **1931**, 12, 593−601.
(26) Shirley, D. A. Phys. Rev. B: Condens. Matter Mater. Phys. **1972**, 5, 4709−4714.
(27) Dovesi, R.; Saunders, V. R.; Roetti, C.; Orlando, R.; Zicovich-Wilson, C. M.; F. Pascale, B. C.; Doll, K.; Harrison, N. M.; Bush, I. J.; D'Arco, P.; Llunell, M.; Causà, M.; Noël, Y. CRYSTAL14 User's Manual; University of Torino: Torino, Italy, 2014.
(28) Perdew, J. P.; Ruzsinszky, A.; Csonka, G. I.; Vydrov, O. A.; Scuseria, G. E.; Constantin, L. A.; Zhou, X.; Burke, K. Phys. Rev. Lett. **2008**, 100, 136406.
(29) Young, R. A. The Rietveld Method; 1st Edition; Oxford University Press: New York, 1993.
(30) Wu, Y.; Lu, G. Phys. Chem. Chem. Phys. **2014**, 16, 4165−4175.
(31) Wang, Y.; Zhao, J.; Zhu, Y.; Zhou, B.; Zhao, X.; Wang, Z. Colloids Surf., A **2013**, 434, 296−302.

(32) Yuvakkumar, R.; Hong, S. I. *Spectrochim. Acta, Part A* **2015**, *144*, 281−286.

(33) Moreira, M. L.; Paris, E. C.; do Nascimento, G. S.; Longo, V. M.; Sambrano, J. R.; Mastelaro, V. R.; Bernardi, M. I. B.; Andrés, J.; Varela, J. A.; Longo, E. *Acta Mater.* **2009**, *57*, 5174−5185.

(34) Oliveira, L. H.; de Moura, A. P.; Mazzo, T. M.; Ramírez, M. A.; Cavalcante, L. S.; Antonio, S. G.; Avansi, W.; Mastelaro, V. R.; Longo, E.; Varela, J. A. *Mater. Chem. Phys.* **2012**, *136*, 130−139.

(35) Ghedia, S.; Locherer, T.; Dinnebier, R.; Prasad, D. L. V. K.; Wedig, U.; Jansen, M.; Senyshyn, A. *Phys. Rev. B: Condens. Matter Mater. Phys.* **2010**, *82*, 024106.

(36) Locherer, T.; Prasad, D. L. V. K.; Dinnebier, R.; Wedig, U.; Jansen, M.; Garbarino, G.; Hansen, T. *Phys. Rev. B: Condens. Matter Mater. Phys.* **2011**, *83*, 214102.

(37) Pereira, A.; Errandonea, D.; Beltrán, A.; Gracia, L.; Gomis, O.; Sans, J.; García-Domene, B.; Miquel-Veyrat, A.; Manjón, F.; Muñoz, A.; Popescu, C. *J. Phys.: Condens. Matter* **2013**, *25*, 475402.

(38) Sarma, B.; Jurovitzki, A. L.; Smith, Y. R.; Mohanty, S. K.; Misra, M. *ACS Appl. Mater. Interfaces* **2013**, *5*, 1688−1697.

(39) Jiang, H.-Y.; Liu, J.; Cheng, K.; Sun, W.; Lin, J. *J. Phys. Chem. C* **2013**, *117*, 20029−20036.

(40) Myung, N.; Ham, S.; Choi, S.; Chae, Y.; Kim, W.-G.; Jeon, J.; Paeng, K.-J.; Chanmanee, W.; de Tacconi, N. R.; Rajeshwar, K. *J. Phys. Chem. C* **2011**, *115*, 7793−7800.

(41) Zhou, S.; Jiang, N.; Zhu, B.; Yang, H.; Ye, S.; Lakshminarayana, G.; Hao, J.; Qiu, J. *Adv. Funct. Mater.* **2008**, *18*, 1407−1413.

(42) Lei, Y.-H.; Chen, Z.-X. *J. Chem. Phys.* **2013**, *138*, 054703.

(43) Debies, T. P.; Rabalais, J. W. *Chem. Phys.* **1977**, *20*, 277−283.